Research paper

Enhanced As(III) transformation and removal with biochar/SnS$_2$/phosphotungstic acid composites: Synergic effect of overcoming the electronic inertness of biochar and W$_2$O$_3$(AsO$_4$)$_2$ (As(V)-POMs) coprecipitation

Ke-Hui Xue [a], Jing Wang [a], Ying Yan [a], Yi Peng [a], Wen-Lei Wang [a,*], Hong-Bo Xiao [a], Chong-Chen Wang [b,*]

[a] College of Science, Central South University of Forestry and Technology, Changsha 410004, China
[b] Beijing Key Laboratory of Functional Materials for Building Structure and Environment Remediation, Beijing University of Civil Engineering and Architecture, Beijing 100044, China

ARTICLE INFO

ABSTRACT

The activation of carbon atoms in biochar is an important approach for realizing the reuse of discarded woody biomass resources. In this work, a strategy for the construction of carbon-based catalysts was proposed with Magnoliaceae root biomass as a carbon source, doped by SnS$_2$ and further decorated with heteropoly acid. The introduction of SnS$_2$ can activate the carbon atom and destroy the electronic inertness of the disordered biochar with 002 planes. In addition, the synergy between the Keggin unit of phosphotungstic acid and biochar/SnS$_2$ can suppress recombination of e$^-$–h$^+$ carriers. The adsorption and photocatalysis experiments results showed that the efficiency of removing As(III) by biochar/SnS$_2$/phosphotungstic acid (biochar/SnS$_2$/PTA) systems was 1.5 times that of biochar/SnS$_2$ systems, and the concentration of total arsenic in the biochar/SnS$_2$/PTA composite system gradually decreased during the photocatalysis process. The formation of As-POMs can simultaneously realize As(III) photooxidation and As(V) coprecipitation. The phase transfer of arsenic by As-POMs could significantly increase the As adsorption capacity. Specifically, the composites achieved the conversion of S atoms at the interface of biochar into SO$_4^{\bullet-}$ radicals to enhance the As(III) photooxidation performance.

1. Introduction

The activation of carbon atoms in biochar, which can participate in biological and nonbiological redox reactions, is still a challenge in the field of reusing discarded woody biomass resources (Yi et al., 2019; Ye et al., 2020; Moon et al., 2017). In particular, biochar with phenazine and quinone groups is considered to be an effective and economical adsorbent for removing heavy metals (Wu et al., 2020; Wang et al., 2019) and other soil pollutants (Roden et al., 2020). The carbon in biochar is in the form of π–π* and the electronic structure is stable, meaning it is not conducive to the transfer or reorganization of electrons (Oh et al., 2018). This phenomenon will limit the applications of biochar in heterogeneous catalytic reactions. Furthermore, it is generally believed that carbon catalysis may date from "active sites" like functional groups (Jiang et al., 2018), structural defects (Klüpfel et al.,

2014), or heteroatom (Li et al., 2020) to achieve regulation toward the carbon skeletons. These carbon networks usually show distinctive spin properties and electronic states. Hence, the modification of heteroatoms on the surface of biochar is an important strategy for building electronic defects to modulate the carbon networks and improve their photo-catalytic performance (Qu et al., 2020; Liu et al., 2010). The N,S-doped porous carbon synthesized using coffee grounds as a carbon source has exhibited an excellent photocatalytic oxidative degradation performance for tetracycline hydrochloride (Huo et al., 2020). It was proven that heteroatom doping can break the electronic inertness of the carbon framework and effectively produce point defects, which play a key role in the process of photocatalytic oxidation.

Oxy-acid ion pollutants like As(III) seriously restricts the sustainable development of human society. With increasing soil environmental pollution, arsenic (As) have been listed as key global targets for

prevention and control (Luo et al., 2019; Dong et al., 2014). In addition, As(III) is easily soluble in water and shows a higher fluidity and toxicity compared to As(V) (Dixit and Hering, 2003; Li et al., 2016). The original biochar exhibits poor adsorption and removal capacity for oxy-acid ion species. In view of the mentioned problems, it is practical to develop a photocatalyst with biochar as a template for redox reactions. Liu et al. (2019b) reported that carbon-sphere@nano-Fe$_3$O$_4$ can significantly accelerate the coordinated photocatalytic As(III) oxidation and Cr(VI) reduction of under visible light irradiation. In addition, Wu et al. (2018) reported that Zn$_3$In$_2$S$_6$ can improve the photocatalytic performance of the carbon nitride by the interfacial contact due to the well-matched conduction band and valence band edge potentials. Generally, the modification of carbon-based catalysts is one of the important measures for improving their interfacial adsorption and photocatalytic ability to remove oxy-acid ion species and expand the application value of carbon catalysts (Navarathna et al., 2019; Sadeghi et al., 2020; Wu et al., 2012; Xi et al., 2019; Yang et al., 2020). The preoxidation of As(III) to As(V) followed by a simple coprecipitation or adsorption method strategy is very important to completely remove them from the environment. Several typical metal sulfides, such as CdS, In$_2$S$_3$ and SnS$_2$, have been studied owing to their obvious visible light performances (Li et al., 2010). Among them, SnS$_2$, an inexpensive, low environmental toxicity and good stable material with a specific CdI$_2$-type layered structure, shows a narrow band gap value of ~2.40 eV (An et al., 2014). It has been proved to be a promising visible light-sensitive photocatalyst in theory and practice (Dashairya et al., 2019; Huang et al., 2019; Liu et al., 2020). And the introduction of SnS$_2$ is expected to adjust the electronic structure of biochar and improve its photocatalytic ability to oxidation of As (III).

Magnolia Wulin is a Magnoliaceae plant self-supported by Central South University of Forestry and Technology in Changsha, Hunan Province, China. And its bark and leaf resources are widely used in the extraction of chemical components and medicinal purposes. The reuse of discarded roots conforms to the concept of environmental protection and resource utilization. Hence, the roots of *Magnolia Wulin* are selected as the source of biochar. In this work, both S and Sn were introduced to overcome the electronic inertness of the carbon network. Meanwhile, the decoration of polyoxometalates (POMs) was selected to improve the interface adsorption capacity. The As(III) was selected to assess the removal ability of the as-prepared biochar/SnS$_2$ decorated with phosphotungstic acid (PTA) composite material, in which the effects of different pH values and competing co-existing ions toward arsenic removal were investigated. In addition, EPR and active radical capture experiments were used to analyze the possible mechanisms of the photocatalytic oxidation of As(III). The exploration of this research was helpful for understanding the redox process of biochar-based composite materials on As(III) species and provided a way to improve the electronic inertness of biochar and expand the application of biochar in the environment.

2. Experimental section

2.1. Synthesis of the photocatalyst

2.1.1. Synthesis of SnS$_2$ doped porous biochar

A suction method was used to make the load enter the pipe wall evenly. First, the biochar, which used Magnoliaceae waste wood from the low-value root biomass of *Magnolia Wulin* as a carbon source, was spread on the Buchner funnel, and a 0.25 mmol SnCl$_4$.5 H$_2$O solution was used several times for rapid filtration. Then, the collected solution slowly passed through the biochar without suction filtration, and the compound was shifted to a 50 mL polytetrafluoroethylene autoclave, which was then kept at 160 °C for 12 h. After the reaction, the autoclave was cooled to an indoor temperature to obtain the product, which was centrifuged at 8000 rpm for 2 min, washed with ethanol and H$_2$O several times, and dried in a vacuum environment at 50 °C for ulterior use.

Then, the obtained solid intermediate product was subjected to a similar procedure, with a liquid phase vulcanization reaction of 0.50 mmol TAA (thioacetamide) as the sulfur source. The obtained composite material was named as biochar/SnS$_2$.

2.1.2. Synthesis of SnS$_2$ doped porous biochar decorated with PTA

In a typical manner, a certain amount of phosphotungstic acid (H$_3$PW$_{12}$O$_{40}$) that was purchased from Sinopharm Chemical Reagent (Shanghai, China) and 100 mg biochar were dispersed in ethanol (10 mL) and kept for 5 min under ultrasonic conditions to make the solution evenly mixed. Then, the mixed system was transferred to a 25 mL Shrek tube. After stirring and heating the obtained compound at 80 °C for 1 h, the compound was subjected to a hydrothermal process at 150 °C for 12 h with a heating rate of 1 °C/min. After the reaction, the Shrek tube was cooled to a room temperature to obtain the solid product, which was collected via centrifugation, washed with ethanol, and dried under vacuum at 50 °C. The as-synthesized products were named biochar/SnS$_2$/PTA-*x*, where *x* is the dose of H$_3$PW$_{12}$O$_{40}$ in terms of molar ratio.

2.2. Characterizations

The microstructure and chemical composition of the as-obtained materials were observed and characterized through scanning electron microscopy (SEM) (JEOL JXA-840A) and transmission electron microscopy (TEM) (JEM-2100 (HR)). The powder X-ray diffraction (XRD) patterns were recorded using a Bruker D8 Advance equipped with Cu−Ka ($\lambda = 0.15406$ nm) for 2θ between 5° and 90° to test the phase and crystal structure of the samples. X-ray photoelectron spectroscopy (XPS) (Thermo Kalpha) was implemented to analyze the chemical environment and chemical state of the element of the biochar/SnS$_2$/PTA-*x* materials. UV–visible light diffuse reflectance spectra (UV–vis DRS) were obtained on a TU-1901 UV-Vis spectrophotometer to estimate the light absorption range of the as-prepared samples in the range of 200–800 nm and with BaSO$_4$ as the reference. The photoluminescence (PL) (Hitachi F-7000) spectra were used to explain the recombination rate of the photogenerated carriers for biochar/SnS$_2$/PTA composites with excitation wavelength of 422 nm. An electron paramagnetic resonance (EPR) analyses (Bruker A300) with a spin trapping of 2,2,6,6-tetramethylpiperidinooxy (TEMPO) and 5,5-dimethyl-1-pyrrolidine N-oxide (DMPO) were performed to capture the holes or free radicals in the photooxidation process of As(III).

2.3. Adsorption and photocatalysis experiments

The photooxidation of As(III) experiments were performed in a 40 mL quartz tube. In a typical test, 30 mg photocatalysts were dispersed in 35 mL As(III) solution ($C_0 = 10$ mg/L) for 30 min to achieve adsorption-desorption equilibrium in the dark. A pre-experiment under dark conditions was performed before the photocatalysis experiments in order to determine whether the system reached adsorption-desorption equilibrium within 30 min. A 500 W xenon lamp with a 420 nm UV cutting filter was used as a visible light source (Perfect Light Co., China). And Xe lamp does not contain ozone. After light treatment, the NaAsO$_2$ solution was collected through the injector with a 0.45 μm disposable filter into a 5 mL centrifuge tube at regular intervals. The solutions were centrifuged at 12,000 rpm for 3 min to remove the photocatalysts powder for further determining the residual As(III) concentrations. Additionally, the As(III) concentrations were acquired through a CHI600E electrochemical workstation analyzer (Shanghai Chenhua Instrument Co., Ltd., China) with a normal three-electrode analysis system. The As(V) concentrations were detected via liquid chromatography-atomic fluorescence spectrometry (LC-AFS) (AFS-8220). Moreover, the influences of pH values as well as co-existing ions like Cl$^-$, NO$_3^-$, CO$_3^{2-}$, SO$_4^{2-}$ and PO$_4^{3-}$ ions on the distribution of arsenic species and the photocatalytic As(III) oxidation were investigated. The pH value was regulated by NaOH or HCl solution with suitable concentrations. The five ions mentioned above came from

the NaCl, NaNO$_3$, Na$_2$CO$_3$, Na$_2$SO$_4$ and NaH$_2$PO$_4$ salts, which were purchased from Sigma-Aldrich.

3. Results and discussion

3.1. The microstructure and crystal structure analysis

Understanding the surface chemistry of the as-prepared biochar/SnS$_2$/PTA composite material will help us investigate the factors affecting the removal of arsenic. The SEM images are shown in Fig. 1a–f. In Fig. 1a, pure biochar exhibited a large specific surface area and a smooth surface. SnS$_2$ was easy to reunite into a flower-like morphology (Fig. 1b), and PTA tended to aggregate into a block-like structure (Fig. 1c). As shown in Fig. 1d–f, the as-obtained biochar/SnS$_2$/PTA composite material by hydrothermal method can effectively prevent the agglomeration of SnS$_2$ and PTA. As expected, the SnS$_2$ nanosheets grew uniformly on the surface of the biochar, and PTA were loaded on the SnS$_2$ nanosheets. The results illustrated that biochar/SnS$_2$/PTA were successfully synthesized using biochar as a direct template. And PTA clusters adhered to the outer surface of biochar/SnS$_2$/PTA, which indicated the formation of interface interactions between the ternary composites. This anisotropic structure can increase the exposure of the active sites to accelerate the photocatalysis performance. Meanwhile, energy dispersive X-ray spectroscopy (EDX) also illustrated the coexistence of C, Sn, S, P, W and O elements (Fig. 1g). The crystallographic structures of the biochar/SnS$_2$/PTA composite were measured via XRD (Fig. 1h). From Fig. 1h, biochar/SnS$_2$/PTA samples showed only a sharp diffraction peak at approximately 26.5°, which was ascribed to the (002) plane of the graphitic structure (Zhang et al., 2020). This phenomenon indicated that the disordered biochar was successfully converted into single-phase graphite carbon. And hydrothermal process caused serious damage to the (102) crystal plane of SnS$_2$ located at 41.9°. Furthermore, the characteristic peaks of the biochar/SnS$_2$/PTA at 2θ values of 14.8°, 28.5°, 32.0° and 49.9° were attributed to the (001), (100), (011) and (110) crystal faces of SnS$_2$ (JCPDS No. 83-1705), respectively, implying that the SnS$_2$ nanosheets were inserted into the interlayer space and then combined with the graphite plane during the pyrolysis of biochar (Liu et al., 2019a). Two new peaks appearing at 36.2° and 39.2° corresponded to the (102) and (103) planes of WS$_2$ (JCPDS No. 08-0237), respectively, revealing that the PTA were successfully decorated on biochar/SnS$_2$ via W–S chemical bonds (Lu et al., 2012). By comparing the (002) crystal plane of the XRD pattern (Fig. 1i), it is noteworthy that the increase in the loading of PTA during the preparation process may promote an improvement in the graphitization degree of biochar, which
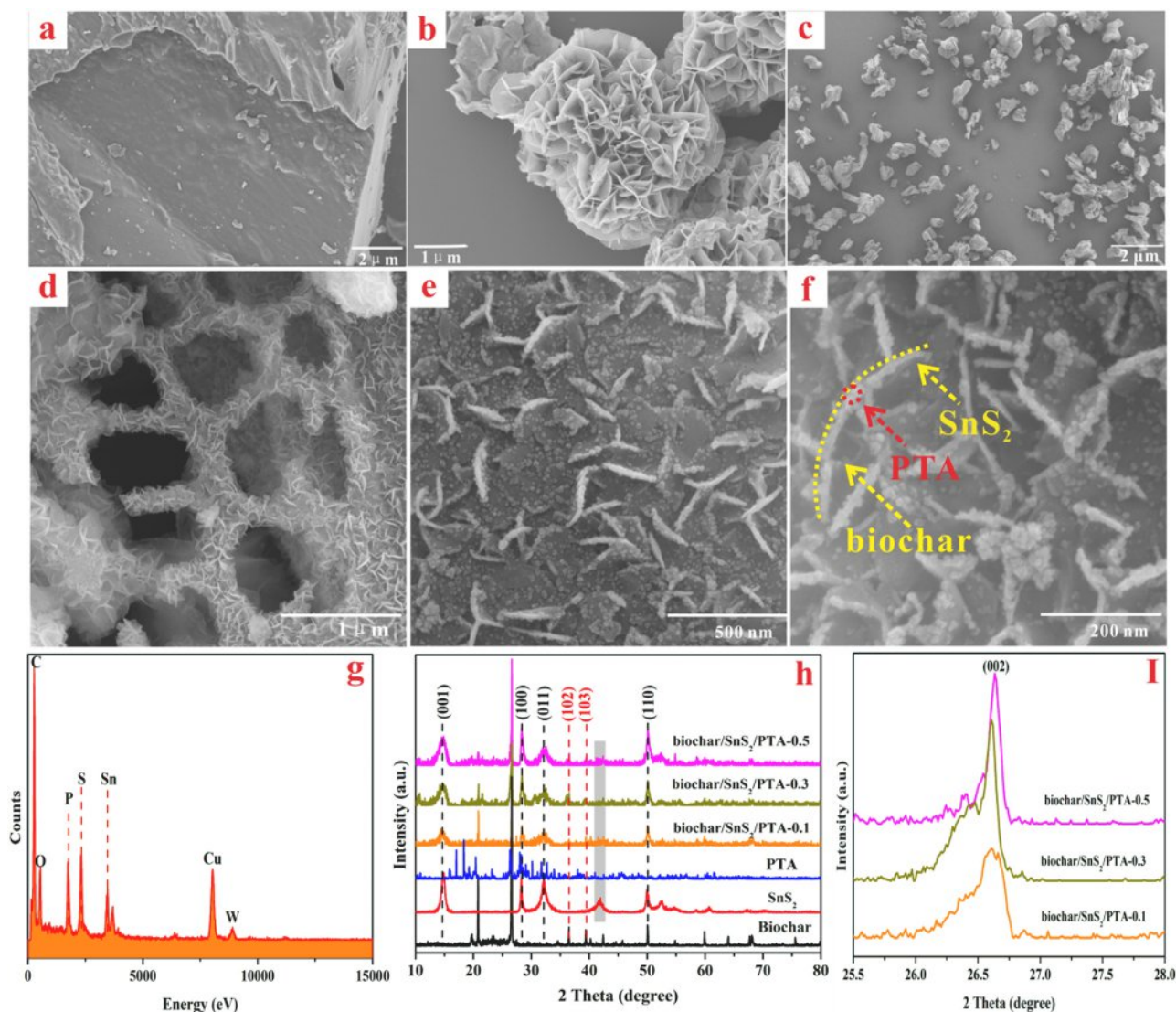

Fig. 1. SEM images of (a) biochar, (b) SnS$_2$, (c) PTA and (d–f) biochar/SnS$_2$/PTA hybrids, (g) EDX spectra analysis jond (h–i) XRD patterns for biochar/SnS$_2$/PTA materials.

was not conducive to disturbing the electronic structure and spin of the sp^2 hybrid carbon atom or the activation of delocalized electrons of carbon atoms.

Fig. 2 shows the TEM images of biochar/SnS$_2$/PTA to evaluate the microstructure and element distribution. From Fig. 2a–c, the microscopic morphology shown by the TEM of biochar, SnS$_2$ and PTA was consistent with the SEM image (Fig. 1a–c). Many micropores were observed in the simple biochar. As displayed in Fig. 2d–e, the PTA particles were decorated on the interface of biochar/SnS$_2$ to design biochar/SnS$_2$/PTA hybrids without any destruction of the biochar or

SnS$_2$ nanosheet structures. The size of the PTA particles is approximately 20 nm. The high-resolution TEM (HRTEM) characterizations of the biochar/SnS$_2$/PTA composites are displayed in Fig. 2f. The interplanar lattice fringes with d-spacings SnS$_2$ being 0.588 nm correlated to the (001) crystal facet, which corresponded well with the XRD analysis (Fig. 1h) (Liu et al., 2019a). The lattice interface between the PTA and biochar/SnS$_2$ was integrated. From the SEM image as illustrated in Fig. 1d, the method of suction filtration can unblock the tube wall of the biochar to favor the Sn and S load in the biochar even onto the tube wall during the process of sample preparation. Additionally, phosphotungstic
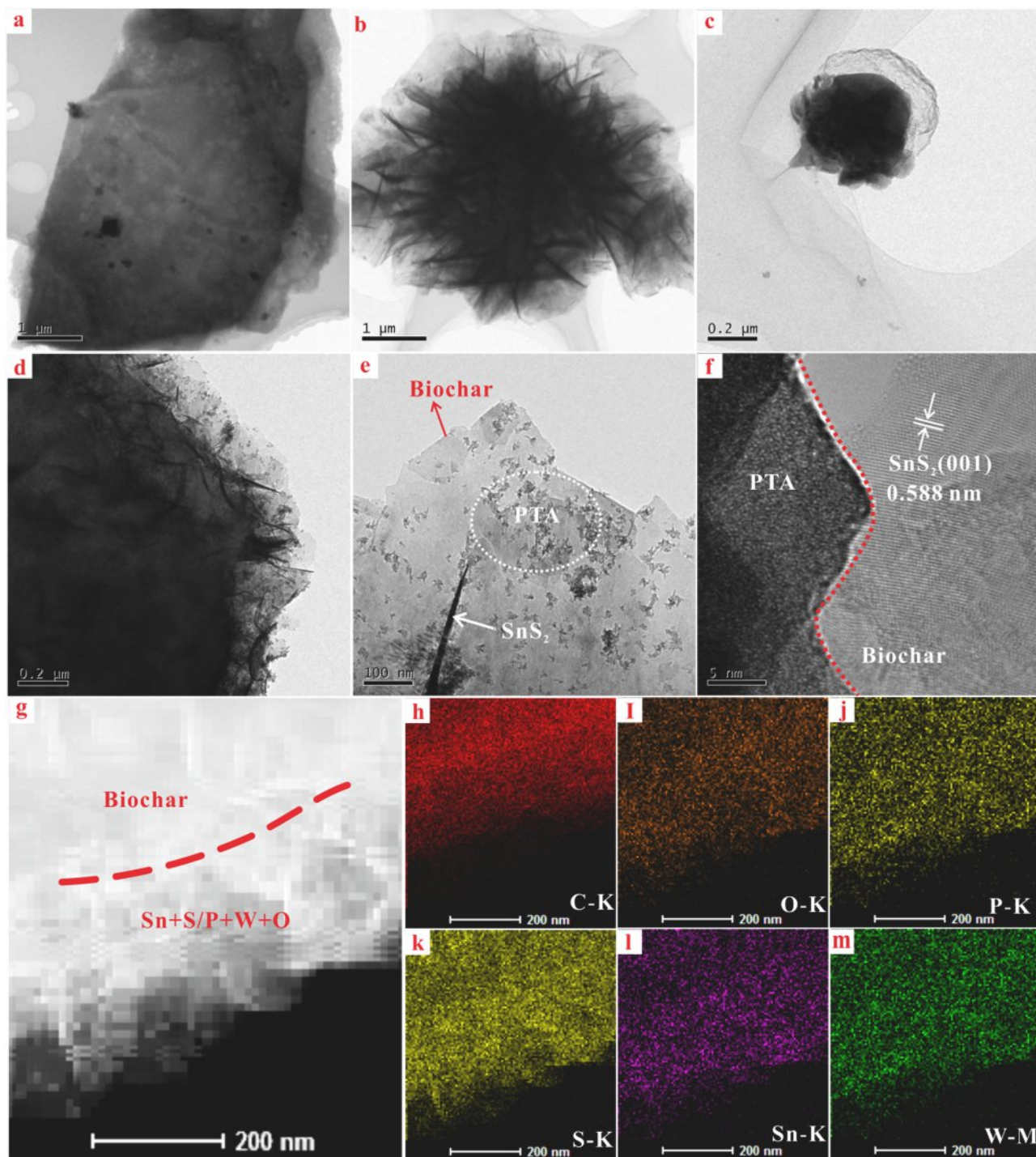

Fig. 2. TEM images of (a) biochar, (b) SnS$_2$, (c) PTA, (d−e) biochar/SnS$_2$/PTA and (f) HR-TEM images of biochar/SnS$_2$/PTA, (g−m) the corresponding EDX mapping of the C, O, P, Sn, S, W elements.

acid (PTA) grew evenly on the surface of biochar/SnS$_2$. TEM−EDX elemental distribution mapping (Fig. 2g–m) for biochar/SnS$_2$/PTA confirmed that C, Sn, S, P, W and O were evenly distributed throughout the scanning section. Delightedly, the TEM images combined with SEM and XRD data confirmed the successful construction of the composite material, in which its structure was as expected with a clear interface.

3.2. Optical performance characteristics

Fig. 3a shows the UV–Vis DRS of the as-obtained samples to characterize the light absorption. Both the SnS$_2$ and biochar/SnS$_2$ composite

Fig. 3. (a) DRS, (b) the related bandgap and (c) PL spectrogram of biochar, SnS$_2$, PTA and biochar/SnS$_2$/PTA.

materials have demonstrated good semiconductor properties in previous studies (Xue et al., 2020). The excellent light response ability is beneficial to improving the utilization of visible light and enhancing the photooxidation or photoreduction ability of oxy-acid ions. As illustrated in Fig. 3a, the biochar/SnS$_2$/PTA-0.1 displayed an absorption edge of approximately 600 nm, and its band gap value was computed to be 1.38 eV. Meanwhile, biochar/SnS$_2$/PTA-0.1 demonstrated an extended the absorption in the visible spectral range and a redshift of the absorption edge compared with SnS$_2$ and PTA, whose absorption edges were at about 650 nm and 400 nm, respectively. And the band gaps of SnS$_2$ and PTA were calculated to be 1.89 eV and 3.00 eV, respectively (Fig. 3b). The introduction of heteroatom S and transition metal Sn had a regulatory effect on the optical absorption properties of the biochar network with the 002 planes. The electronic state of S affected the edge of the conduction band, and the band gap of the composite material was decreased (Zhu et al., 2019). However, the optical response intensity of the biochar/SnS$_2$/PTA composites in the visible light range declined as the quantity of PTA increased. This result was ascribed to the coverage of phosphotungstic acid reducing the light response area of biochar/SnS$_2$. To further characterize the optical properties of the composite material, the as-prepared material was subjected to PL detection (Fig. 3c) to test the recombination rate of the photogenerated electron hole. Obviously, the PL intensity of biochar/SnS$_2$/PTA hybrid materials was significantly depressed contrast with biochar, SnS$_2$ and PTA, which illustrated that the construction of ternary composite materials was beneficial to inhibit the recombination of photo-induced carriers and accelerate the separation of electron-hole pairs. And the biochar/SnS$_2$/PTA-0.1 material exhibited a lower PL peak, which was attributed to the Keggin unit of the PTA being used as an electron trap to enhance the electron trapping ability. Meanwhile, composites based on –C˭Sn–S bonds can activate the π–π* network of biochar in order to improve the utilization of captured electrons. As the mass ratio of PTA to biochar/SnS$_2$ further increased, it was not conducive to the separation of photogenerated electrons and hole pairs, which due to the fact that the Keggin structure of PTA was favorable to trapping too many electrons (Li et al., 2014). Significantly, PL characterization combined with a DRS spectrum analysis demonstrated that biochar/SnS$_2$/PTA-0.1 composites can prolong the service life of h$^+$ and activate the hydroxyl groups to •OH groups on the surface of biochar.

3.3. Photocatalytic property evaluation

3.3.1. Photocatalytic conversions of As(III) and co-precipitation of As(V)

Experiments on the photooxidation As(III) were performed to evaluate the removal efficiency of as-synthesized biochar/SnS$_2$/PTA samples for oxy-acid ion pollution under visible light conditions at room temperature. The adsorption and photocatalytic oxidation performance of the as-prepared samples for arsenite were compared and studied. Among the results shown in Fig. 4a–d, the adsorption effects of the composite material on arsenite and arsenate were first explored before studying the photocatalytic conversion of As(III). As exhibited in Fig. 4a, the maximum adsorption capacity for pure As(III) was approximately 2.2 mg/L, while that for As(V) was 8.1 mg/L, which is 4 times the adsorption capacity toward As(III). This result indicated that the removal efficiency of As(V) was more significant compared to the pure adsorption of As(III), which was due to the coprecipitation between arsenate and the heteropoly acid. The phase transfer of arsenic could lead to significant increase of As adsorption capacity; therefore, the photocatalytic conversion of arsenite was implemented to achieve a low-toxicity treatment of arsenic, with the results displayed in Fig. 4b. The concentration of As(III) gradually decreased in the photocatalysis system of biochar/SnS$_2$/PTA. Among them, it took approximately 90 min for biochar/SnS$_2$/PTA-0.1 to remove arsenite with concentration of 10.0 mg/L. While in the biochar/SnS$_2$/PTA-0.3 and biochar/SnS$_2$/PTA-0.5 systems, the arsenite removal efficiencies were 90% and 80% within 90 min, respectively. This phenomenon can be contributed to that the
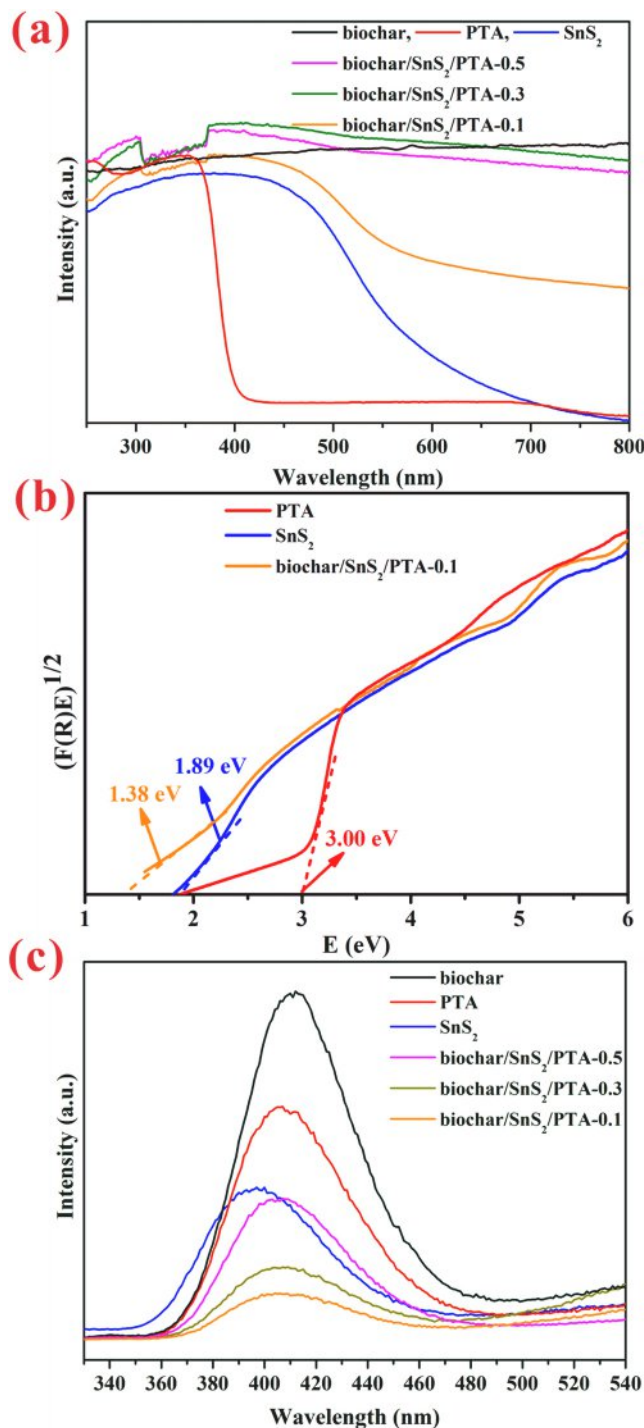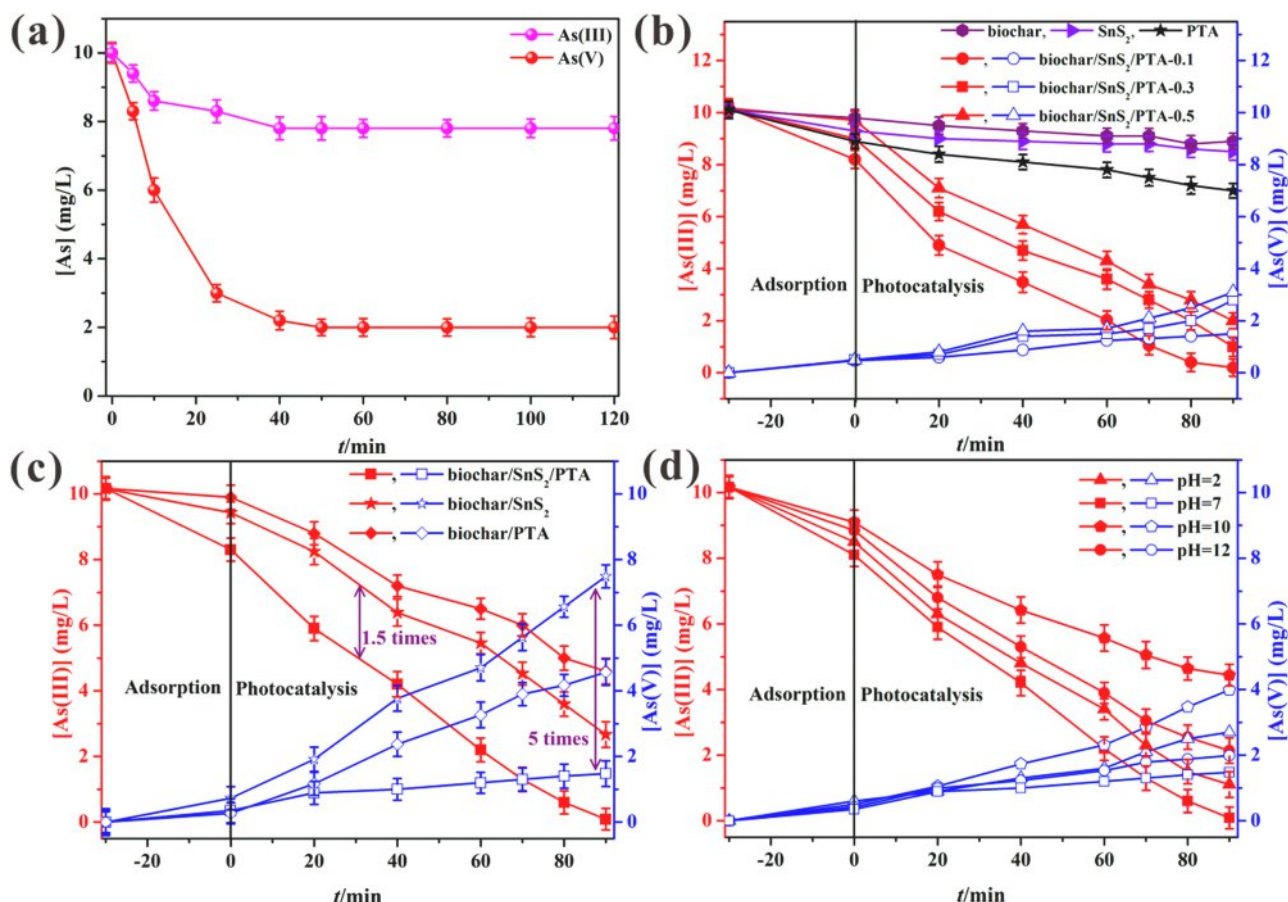
Fig. 4. (a) Adsorption performance of As(III) and As(V) via biochar/SnS$_2$/PTA. (b) Oxidation conversion performance toward As(III) and change in the concentration of As(V) in the presence of biochar, SnS$_2$, PTA and biochar/SnS$_2$/PTA. (c) Comparison of the concentration changes of As(III) and As(V) in the biochar/SnS$_2$, biochar/PTA and biochar/SnS$_2$/PTA systems (experimental conditions: M (photocatalyst) = 30 mg, [As(III)]$_0$ = 10 mg/L, pH = 7.0, and λ > 420 nm). (d) Effect of the initial pH on biochar/SnS$_2$/PTA-0.1 for As(III) and As(V).

high loading of PTA covered the active sites of photocatalysis and subsequently inhibited the photooxidation of As(III). In addition, compared with the biochar/SnS$_2$/PTA composite materials, the adsorption and photocatalytic conversion ability of pure biochar to As(III) was very poor (Xue et al., 2020), which highlighted that the introduction of S and Sn had the synergic effect of activating electrons on the carbon network of biochar and contributed to the photocatalysis reaction of As(III). And SnS$_2$ and PTA alone had inferior ability to remove As(III). Luckily, although the concentration of As(V) was increased, the concentration of the total As in the biochar/SnS$_2$/PTA system obviously reduced ([As (III)]+ [As(V)] < Total [As]). Therefore, the conversion of arsenite and the coprecipitation of arsenate occurred simultaneously in the biochar/SnS$_2$/PTA system.

As illustrated in Fig. 4c, to verify the arsenic precipitation effect of PTA, photocatalytic experiments of the biochar/SnS$_2$, biochar/PTA and biochar/SnS$_2$/PTA systems were performed. The results showed that the efficiency of removing As(III) and As(V) using the biochar/SnS$_2$/PTA system was 1.5 and 5 times that of the biochar/SnS$_2$ systems, respectively, and the concentration of total arsenic in the biochar/SnS$_2$/PTA composite system gradually decreased during the photocatalysis process. Compared with biochar/SnS$_2$, biochar/PTA had poor photocatalytic ability for As(III), but its removal performance for As(V) was better, which further revealed the necessity of constructing ternary composite materials. SnS$_2$ improved the photocatalytic performance of the material, and PTA played a role in arsenic precipitation. After a comparative analysis, the as-prepared hybrids decorated with PTA can efficiently photooxidize As(III) to As(V). The phase transfer of arsenic by As-POMs could significantly increase the As adsorption capacity.

Furthermore, the Keggin unit of the PTA facilitated the transfer of electrons and reduced the recombination rate of photogenerated carriers, which can simultaneously realize As(III) photooxidation and As(V) coprecipitation to provide a potential platform for the effective removal of As.

3.3.2. Effect of pH on arsenic removal

To estimate the effect of the initial pH of the system on the photooxidation of As(III) and the precipitation of As(V), the removal of As(III) and As(V) by the photocatalyst was investigated at initial pH values of 2, 7, 10, and 12, and the results are displayed in Fig. 4d. At pH = 7, the biochar/SnS$_2$/PTA-0.1 system exhibited a better removal ability for both As(III) and As(V), while the system's ability to remove arsenic was reduced under acidic conditions. Similarly, with the gradual increase in the pH under alkaline conditions, the capacity of the system to remove arsenic gradually decreased. This result was mainly related to the distribution of arsenic species at different pH values. The H$_3$AsO$_3$ and H$_2$AsO$_3^-$ species are the dominant As(III) species with pH ranges of 2–9.2 and 9.2–10.7, respectively. As(V) exists in H$_2$AsO$_4^-$ at pH < 7, while the HAsO$_4^{2-}$ species increase rapidly as the pH increases from 7 to 12 (Deng et al., 2010). The presence of H$^+$ at pH = 2 can protonate the OH groups into OH$_2^+$, which will negatively affect the generation of •OH radicals and inhibit the photooxidation progress of As(III). In an alkaline environment, the deprotonation of the OH group was not conducive to adjusting the electronic band gap and improving the ion conductivity (Zhang et al., 2009). This phenomenon was adverse to the rapid transfer of electrons in the Keggin unit of the phosphotungstic acid, which in turn had a negative effect on the generation and transfer of photogenerated

carriers. Moreover, the electrostatic repulsion between the $H_2AsO_3^-$ or $HAsO_4^{2-}$ species and the catalyst surface was detrimental to the adsorption of As(III)/As(V) at pH = 10 or 12. Satisfactorily, at pH = 7, As(III) exists as a nonelectrical H_3AsO_3 species and does not affect the production of active free radicals, which is beneficial for accelerating the transfer of arsenic species between the interfaces and the photooxidation process (Imran et al., 2020).

3.3.3. Ion competition analysis

There are anions in the environment, such as chloride, nitrate, carbonate, sulfate, silicate and phosphate, which may hamper the removal of arsenic. Therefore, the effects of Cl^-, NO_3^-, CO_3^{2-}, SO_4^{2-} and PO_4^{3-} competitive ions on the photocatalytic conversion of As(III) and the adsorption of arsenic on the biochar/SnS$_2$/PTA-0.1 system were explored. As exhibited in Fig. 5a, it was explicitly discovered that the impact of coexisting Cl^-, NO_3^-, CO_3^{2-} and SO_4^{2-} ions on the photooxidation of As(III) by biochar/SnS$_2$/PTA-0.1 was negligible, even though the original concentration was up to 100 mg/L. However, in the case of the coexistence of 100 mg/L of PO_4^{3-}, the photocatalytic efficiency of the photocatalyst to As(III) was reduced to 78.8%. This phenomenon occurred because PO_4^{3-} and arsenite had similar ionic structures and competed with one another for photocatalytic active sites (Meng et al., 2000). Furthermore, SO_4^{2-} exhibited little effect on the removal of the total arsenic. In the presence of NO_3^- and CO_3^{2-}, the total arsenic removal efficiency was reduced from 99.5% to 59.9% and 75.1%, respectively. The existence of Cl^- had an obvious inhibitory effect on the removal of total As. Therefore, the as-prepared composites can be suitable for the removal of arsenic pollution in overlying water of paddy soil under flooding conditions. By comparison, PO_4^{3-} ions greatly restrained the total arsenic species removal, and the removal capacity of arsenic decreased from 99.5% to 19.8%. As expected, the analogical tetrahedral structure caused PO_4^{3-} to easily contend with arsenic species and build inner-sphere compounds on the surface of biochar/SnS$_2$/PTA-0.1, which resulted in the decline of arsenate precipitation and damping of the arsenic removal ability (Rahnemaie et al., 2007; Kolarik et al., 2018). Therefore, the presence of anions was not conducive to the adsorption of arsenate after photocatalysis, and the interference of these anions needed to be eliminated in the process of removing arsenic from actual water.

3.4. Durability and reusability of the photocatalysts

The durability and repeatability of the photocatalyst exhibits a significant indicative value for its practical use prospects. As demonstrated in Fig. 5b, the reproducibility of biochar/SnS$_2$/PTA-0.1 in the cyclic photooxidation experiments of As(III) and As(V) was discussed. After each cycle experiment, the hydroxyl groups on the surface of the biochar/SnS$_2$/PTA composite material were passivated and the active sites were occupied, leading to efficient desorption of arsenic species. Therefore, the exhausted composite material was placed in 0.1 M NaOH solution and shaken for 1 h to achieve regeneration. The regenerated biochar/SnS$_2$/PTA was then used in the next As(V) removal experiment. The biochar/SnS$_2$/PTA-0.1 photocatalyst can be used repeatedly at least 5 times without evident inactivation of the photocatalytic performance for As(III) and As(V), which revealed its favorable repeatability and satisfactory prospects in practical applications.

3.5. As(V) species co-precipitation mechanism

Different analysis and characterization methods were used to further explore the possible co-precipitation mechanism during the experiment. Noticeably, as illustrated in Figs. 6a, (4E)-4-(2-hydroxybenzylideneamino)-1,2-dihydro-2,3-dimethyl-1-phenylpyrazol-5-one can act as a fluorescent probe to visually display the change trend of the solubility of the arsenic solution under irradiation with a 365 nm ultraviolet lamp (Lohar et al., 2013). From Fig. 6b, the fluorescence signal of the probe and the arsenic solution gradually weakened until there was no fluorescence signal. This phenomenon intuitively elaborated the gradual decrease of the arsenic concentration in the aqueous solution during the photocatalysis process. Moreover, the sample after photocatalysis was characterized by XRD. As shown in Fig. 6c, two new crystal planes appeared in the XRD spectrum after photocatalysis, corresponding to the (102) and (311) crystals of the $W_2O_3(AsO_4)_2$ (As-POM) precipitation (JCPDS No. 27-0912). In Fig. 6d–e, the 0.365 nm and 0.390 nm lattice spacings conformed to the (311) and (102) crystal faces of the As-POMs composites, respectively, as explained through the XRD measurement (Fig. 6c). The TEM and HR-TEM techniques further verified the formation of the As-POMs to realize the coprecipitation of the As (V) species. In other words, As(III) was oxidized to As(V) by photocatalysis, and then As(V) was co-precipitated with phosphotungstic acid in the system. And the formation of As-POMs can realize the phase transfer of arsenite and coprecipitate arsenate to achieve the efficient removal of arsenic species in an aqueous solution.

3.6. Mechanism of photocatalytic conversion of As(III)

The XPS detections for the biochar/SnS$_2$/PTA composites before and after photocatalysis are shown in Fig. 7. The high-resolution spectra of
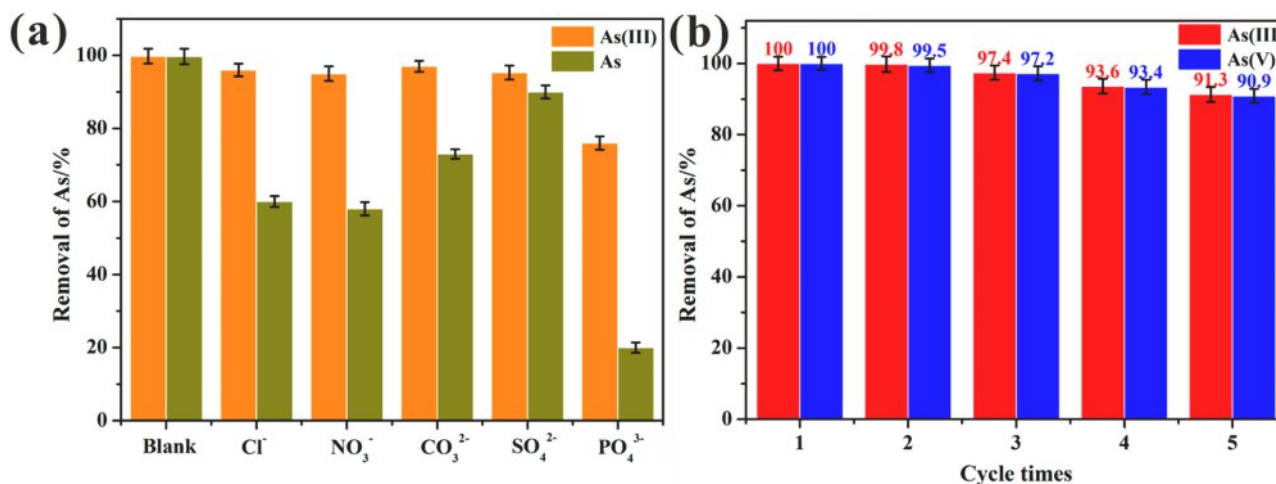
Fig. 5. (a) Effect of coexisting ions on biochar/SnS$_2$/PTA-0.1 for As(III) and As removal. (b) Repeatability and recyclability of the as-obtained biochar/SnS$_2$/PTA-0.1 photocatalysts for the conversion of As(III) and the precipitation of As(V) (experimental conditions: M (photocatalyst) = 30 mg, [As(III)]$_0$ = 10 mg/L, pH = 7.0, and λ > 420 nm).
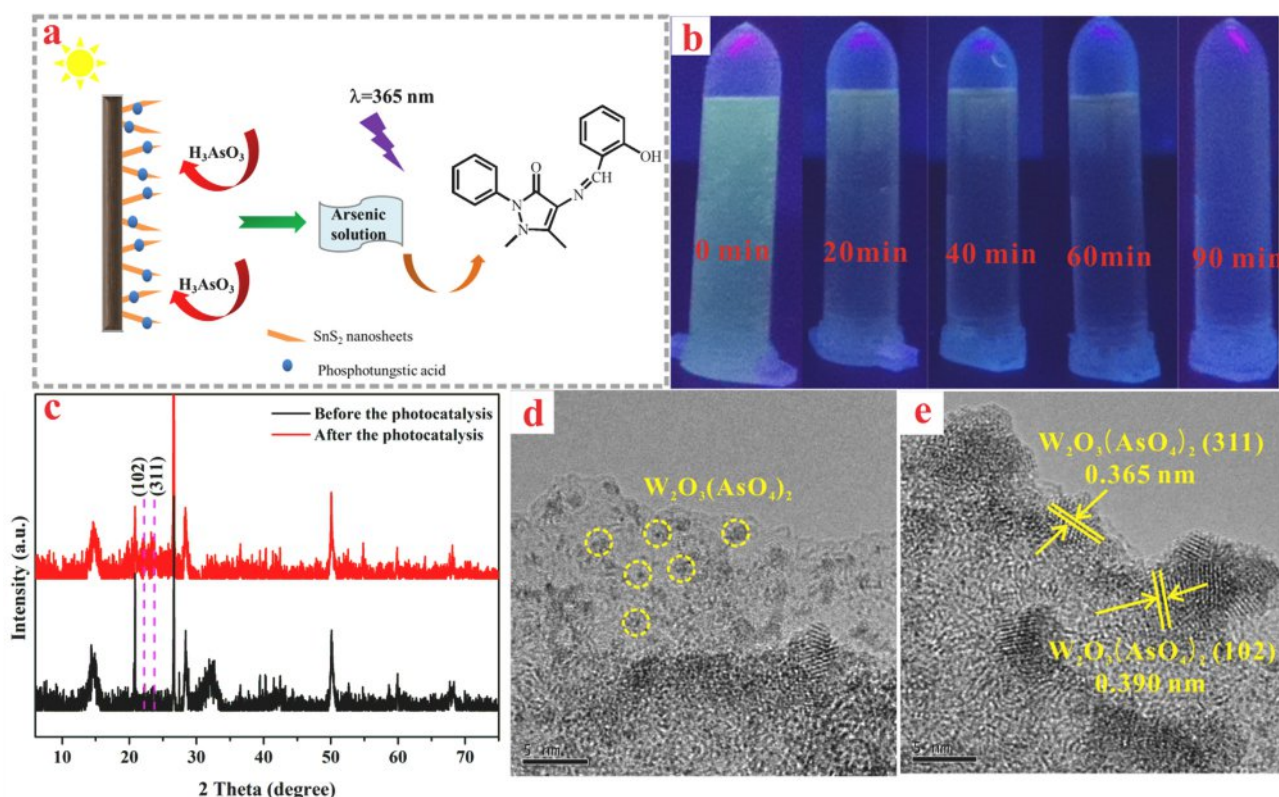
Fig. 6. (a) Schematic diagram of (4E)-4-(2-hydroxybenzylideneamino)-1,2-dihydro-2,3-dimethyl-1-phenylpyrazol-5-one fluorescent probe interacting with an arsenic solution. (b) Fluorescence image of the arsenic solution with the probe. (c) Comparison of the XRD spectra of biochar/SnS$_2$/PTA-0.1 before and after photocatalysis. (d) TEM and (e) HR-TEM of As-POMs after photocatalysis.

the C1s energy region (Fig. 7a) can be deconvoluted into four primary ingredients at binding energies of 284.7, 285.4, 286.6 and 289.2 eV, correlating to the sp^2-bonded carbon, C–S bonds of C, carbonyl carbon (C=O), and carboxyl carbon (O=C=O), respectively. This phenomenon confirmed the exposure of oxygen-containing functional groups of single-phase carbon. The C–S bonds explained that some S heteroatoms were successfully embedded on the graphite carbon layer. Obviously, the XPS data of C1s after the photocatalysis reaction underwent major changes. The strength of the C–S bond increased and shifted to a lower binding energy of 284.8 eV. This phenomenon indicated that the introduction of sp^3 hybrid S helped attract electrons and break the electronic inertia of the carbon network. The carbon skeleton was activated during the photocatalysis process, which was conducive to the efficient progress of the reaction. The O 1 s spectrum (Fig. 7b) of the sample displayed four main signals at 531.1, 531.7, 532.3 and 533.0 eV, indexing to the W–O–W, C–O–H, W–O–P, and W–O–H groups, respectively (Li et al., 2014). Meanwhile, the negative transfer of these four chemical bonds may be due to the high-efficiency electron trap structure of PTA, which exhibited a high electron trapping capacity. The binding energy values of W 4 f (Fig. 7e) at 36.5 and 38.6 eV (before photocatalysis) and after photocatalysis at 36.3 and 38.4 eV corresponded to W 4 f$_{7/2}$ and W 4 f$_{5/2}$, respectively, which are typical for the W(VI) chemical state of the Keggin unit structure. It is worth noting that the shift of the W 4 f binding energy implied the formation of new W-containing chemical bonds after photocatalysis (Zhang et al., 2012). Additionally, the two obvious peaks of the S 2p spectrogram (Fig. 7c) located at 162.1 and 163.2 eV were attributed to Sn−S and C=Sn–S bonds, which showed that there was a chemical interaction between biochar and SnS$_2$ (Dai et al., 2019). Fig. 7d showed the region of Sn 3d, in which the characteristic peaks at 487.1 and 495.6 eV were assigned to Sn 3d$_{5/2}$ and Sn 3d$_{3/2}$, respectively. Obviously, the remarkable peak of the As 3d analysis appeared at 45.8 eV (Fig. 7f). This peak showed that arsenic only existed as an As(V) species after photocatalysis and further

explained that the as-obtained composite material exhibited a significant oxidation effect on arsenite in an aqueous solution. An analysis and comparison of the XPS spectra before and after photocatalysis demonstrated that the introduction of S can interfere with π–π* carbon sp^2 hybridization to activate the carbon atom (Tian et al., 2016). Noticeably, POMs with efficient electron trap structures can act as a bridge to accelerate the electron transfer during the photooxidation process on As (III), which helps to reduce the recombination efficiency of photogenerated carriers and improve the catalytic efficiency of the photocatalyst. Therefore, the introduction of S and PTA was beneficial for improving the electronic performance of carbon-based catalysts and expanding their application prospects in the field of catalysis.

Free radical trapping experiments and the EPR spin-trap technique were performed on the as-induced biochar/SnS$_2$/PTA-0.1 materials. Fig. 8a shows the inhibitory effects of p-benzoquinone (BQ, 0.5 mM) (Han et al., 2019; Huang et al., 2019; Ye et al., 2019), disodium ethylenediaminetetraacetate (EDTA-2Na, 5 mM) and tertiary butanol (t-BuOH, 1 mM) on the photooxidation of As(III) in composites. The As (III) oxidation rate was slightly inhibited by appending the BQ scavenger, suggesting that •O$_2^-$ radicals had little effect on the photooxidation process (Eq. 1) (Xu et al., 2005; Deng et al., 2019). After adding EDTA-2Na, the oxidation efficiency of As(III) dropped from 99.5% to 44.7%, which implied that h$^+$ played a more significant role. In contrast, •OH radicals exhibited the greatest impact on the photocatalytic oxidation of As(III), with the oxygenation efficiency being reduced from 99.5% to 18.7% by adding t-BuOH (Eq. 2). This result showed that •OH radicals and h$^+$ cooperate to participate in the oxidation reaction of As (III), of which •OH radicals were the dominant active species.

In previous research work, it has been explored that the E$_{CB}$ and E$_{VB}$ of biochar are −0.53 V and +1.70 V, respectively, while the E$_{CB}$ and E$_{VB}$ of SnS$_2$ are −0.69 V and +1.28 V, respectively (Xue et al., 2020). Furthermore, the E$_{CB}$ and E$_{VB}$ of phosphotungstic acid are 0.22 V and 3.70 V, respectively (Heng et al., 2016). As an efficient electron trap,
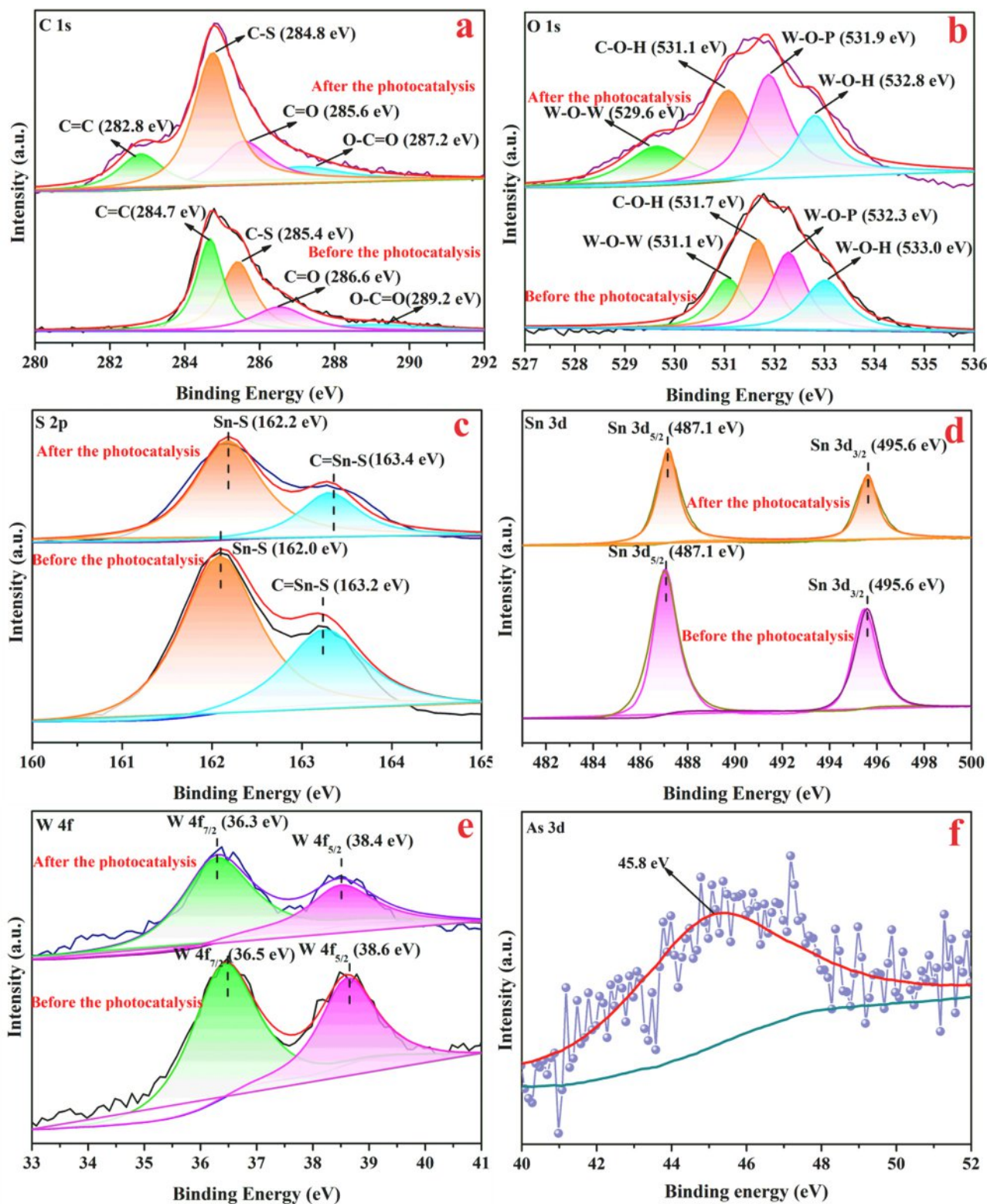
Fig. 7. XPS spectra of biochar/SnS$_2$/PTA: (a) C 1 s, (b) O 1 s, (c) S 2p, (d) Sn 3d, (e) W 4 f and (f) As 3d spectra.

heteropoly acid has a strong ability to capture electrons, so electrons can be transferred from the CB of biochar and SnS$_2$ to the CB of heteropoly acid. Because electrons are trapped in the underfilled W 5d orbital (Li et al., 2014; Lu et al., 2012), the recombination rate of photogenerated electrons and holes is reduced. Furthermore, holes are transferred from the VB of PTA to the VB of biochar and SnS$_2$, and the holes can interact with OH groups or arsenic during the transfer process (Balati et al.,

2020; Zuo et al., 2019; Jiang et al., 2015). Based on the above analysis, a diagram of the electron transfer path in composite materials was proposed, which was helpful for analyzing the mechanism of the photocatalytic process (Fig. 8e).

The synergistic effect of the Keggin unit on biochar/SnS$_2$ hindered the recombination of e$^-$–h$^+$ pairs because the electrons were immobilized in the unfilled W 5d orbital of the Keggin structure, which was
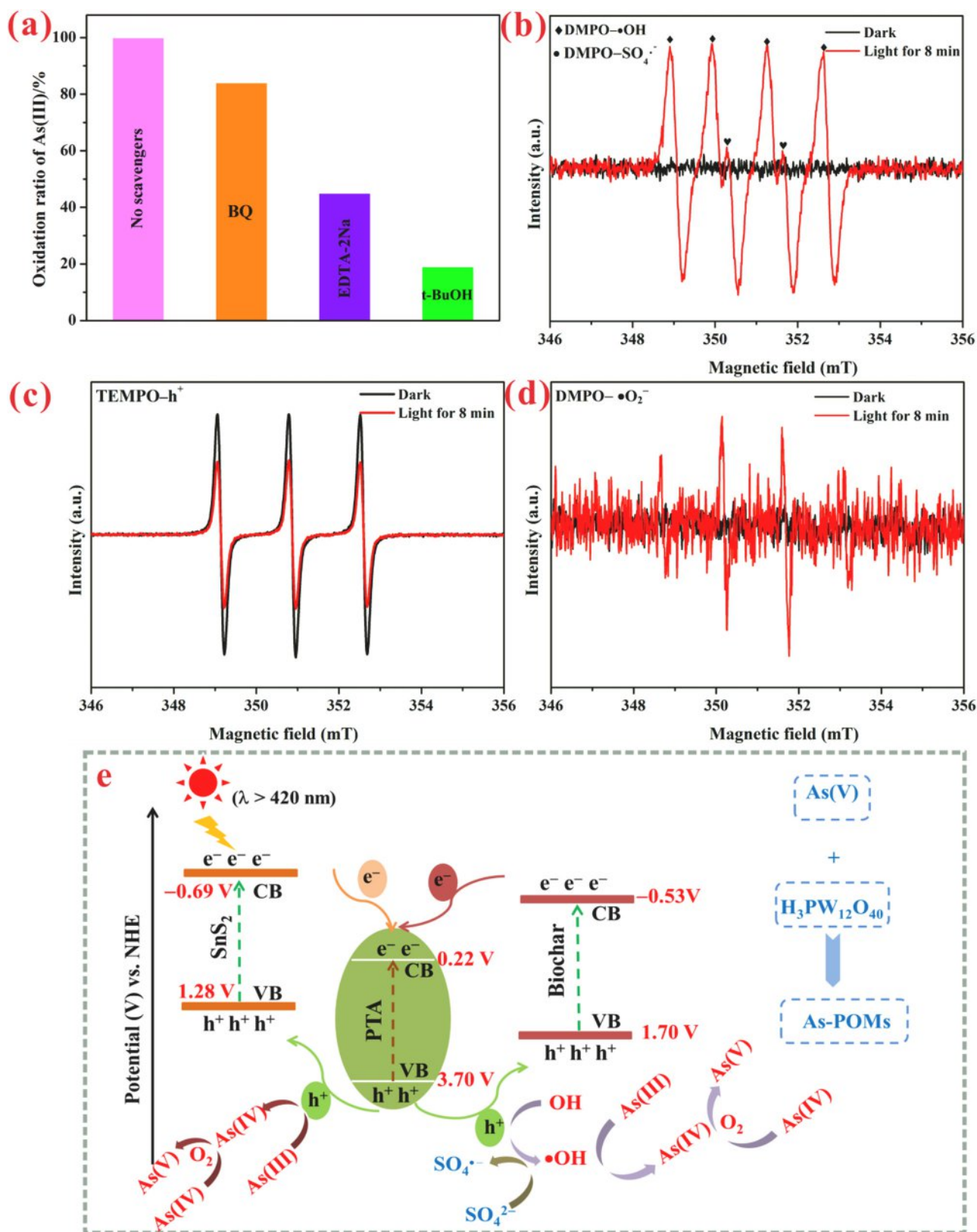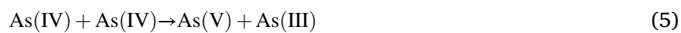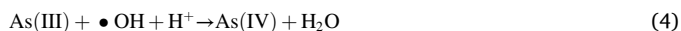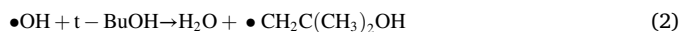
Fig. 8. (a) Trapping experiments of photooxidation of As(III) by adding different scavengers to the biochar/SnS$_2$/PTA-0.1 composite. Typical ESR spectra of (b) DMPO−•OH and DMPO−SO$_4^{•-}$, (c) TEMPO−h$^+$ and (d) DMPO−•O$_2^-$ adducts in the biochar/SnS$_2$/PTA-0.1 system at pH 7.0. (e) The proposed charge transfer pathways and photocatalytic conversion mechanism for As(III) on the biochar/SnS$_2$/PTA-0.1 composites under visible-light irradiation.

beneficial to prolonging the lifetime of the photogenerated holes in the VB of phosphotungstate. As the VB energy level of the phosphotungstic acid (+3.70 V vs NHE) was higher than the redox potential of •OH/OH⁻ (+2.38 V vs NHE) (Zhang et al., 2013), the holes interacted with surface OH groups and generated surface-associated •OH radicals in aqueous media (Eq. 3). The oxidation of As(III) via •OH groups resulted in the generation of As(IV), which were disproportionated to produce As(V) and As(III) (Eqs. 4–5) (Xu et al., 2005). As(IV) can also undergo oxidation through dissolved O_2 to yield As(V) (Eq. 6). Meanwhile, the existence of the DMPO–$SO_4^{\bullet-}$ signals (Fig. 8b) illustrated that the composites achieved the conversion of S atoms at the interface of biochar into $SO_4^{\bullet-}$ radicals. The S species on the surface of biochar can be oxidized by •OH radicals into SO_4^{2-} species (Shi et al., 2020), which can be transferred into $SO_4^{\bullet-}$ radicals under the action of visible light. This phenomenon illustrated that $SO_4^{\bullet-}$ radicals assisted the in photocatalysis process dominated by •OH radicals.

In Fig. 8c, the TEMPO–h^+ signals changed significantly after 8 min of light, revealing that TEMPO–h^+ played an important role in the photocatalysis process, which was consistent with the results of the free radical trapping experiments (Fig. 8a). Since the valence band potential of the phosphotungstic acid (+3.70 V vs NHE) was more positive than the $E^\ominus$ of As(III)/As(IV) (+2.4 V vs NHE) (Kläning et al., 1989), the holes displayed the capacity to oxidize As(III) to As(IV) (Eq. 7). Importantly, the heteroatom S, with a high electronegativity and a large electron density, can disturb the electronic structure and spin of the sp^2 hybrid carbon atom, which can activate the carbon atom and break the electronic inertness of the carbocatalyst. This phenomenon was more conducive to the separation of photogenerated carriers. Similarly, once As(IV) appeared, they were immediately converted to As(V) by the dissolved oxygen in the system (Eq. 6). Additionally, as displayed in Fig. 8d, the DMPO–•O_2^- signals were inconspicuous compared with the DMPO–•OH and TEMPO–h^+ signals. And the redox potential of •O_2^-/H_2O_2 is only 1.71 V vs NHE (Wardman, 1989), which is lower than the $E^\ominus$ of As(III)/As(IV) (+2.4 V vs NHE). This phenomenon revealed that •O_2^- can hardly oxidize As(III) into As(IV). According to the above analysis, the •OH, •SO_4^- and h^+ free radicals synergistically participated in the process of photocatalytic As(III) oxidation, indicating that the as-prepared composite material can achieve efficient As(III) removal. This work can provide potential platforms for the nontoxic treatment of arsenic solutions with biochar-based catalysts, which is conducive to expanding the practical application value and prospects of biochar.

$$BQ + \bullet O_2^- \rightarrow \bullet BQ^- + O_2 \tag{1}$$

$$\bullet OH + t-BuOH \rightarrow H_2O + \bullet CH_2C(CH_3)_2OH \tag{2}$$

$$h^+ + OH^- \rightarrow \bullet OH \tag{3}$$

$$As(III) + \bullet OH + H^+ \rightarrow As(IV) + H_2O \tag{4}$$

$$As(IV) + As(IV) \rightarrow As(V) + As(III) \tag{5}$$

$$As(IV) + O_2 \rightarrow As(V) + \bullet O_2^- \tag{6}$$

$$As(III) + h^+ \rightarrow As(IV) \tag{7}$$

4. Conclusions

In this study, the strategy of SnS_2 introduced and phosphotungstic acid decorated on the surface of biochar with 002 planes based on two-step suction filtration was proposed. The modification of the as-prepared biochar/SnS_2/PTA composites exhibited a uniform morphology and load. POMs and biochar/SnS_2 were combined through W–S bonds. POMs with efficient electron trap structures can accelerate electron transfer during the process of photooxidation on As(III). This helped to reduce the recombination efficiency of photogenerated carriers and

improve the catalytic efficiency of the photocatalyst. The composites displayed excellent photooxidation and photoreduction properties for oxy-acid ion pollutants, including arsenite and dichromate. At pH = 7, the composite system displayed a better removal performance for both arsenite and arsenate. As(III) exists as a nonelectrical H_3AsO_3 species with pH = 7 and does not affect the production of active free radicals. The impact of coexisting Cl^-, NO_3^-, CO_3^{2-} and SO_4^{2-} ions on the photooxidation of As(III) was negligible. Moreover, PO_4^{3-} had a smaller effect on the photocatalytic oxidation of As(III) compared to the adsorption of As(V). This phenomenon was because the formation of As-POMs can simultaneously realize the phase transfer of arsenite and coprecipitate arsenate to achieve the efficient removal of arsenic species in an aqueous solution. Furthermore, the •OH, $SO_4^{\bullet-}$ and h^+ free radicals synergistically participated in the process of photocatalytic As(III) oxidation, of which •OH radicals were the dominant active species. As a result, this work can provide a valuable platform to expand the practical application value and prospects of biochar, which is conducive to the sustainable development of the ecological environment.

CRediT authorship contribution statement

Declaration of Competing Interest

The authors declare that they have no known competing financial interests or personal relationships that could have appeared to influence the work reported in this paper.

Acknowledgments

References

An, X., Yu, J., Tang, J., 2014. Biomolecule-assisted fabrication of copper doped SnS_2 nanosheet–reduced graphene oxide junctions with enhanced visible-light photocatalytic activity. J. Mater. Chem. A 2, 1000–1005.

Balati, A., Matta, A., Nash, K., Shipley, H.J., 2020. Heterojunction of vertically aligned MoS_2 layers to hydrogenated black TiO_2 and rutile based inorganic hollow microspheres for the highly enhanced visible light arsenic photooxidation. Compos. Part B Eng. 185, 107785.

Dai, K., Lv, J., Zhang, J., Liang, C., Zhu, G., 2019. Band structure engineering design of g-C_3N_4/ZnS/SnS_2 ternary heterojunction visible-light photocatalyst with ZnS as electron transport buffer material. J. Alloy. Compd. 778, 215–223.

Dashairya, L., Sharma, M., Basu, S., Saha, P., 2019. SnS_2/RGO based nanocomposite for efficient photocatalytic degradation of toxic industrial dyes under visible-light irradiation. J. Alloy. Compd. 774, 625–636.

Deng, S., Li, Z., Huang, J., Yu, G., 2010. Preparation, characterization and application of a Ce–Ti oxide adsorbent for enhanced removal of arsenate from water. J. Hazard. Mater. 179, 1014–1021.

Deng, F., Lu, X., Luo, Y., Wang, J., Che, W., Yang, R., Luo, X., Luo, S., Dionysiou, D., 2019. Novel visible-light-driven direct Z-scheme CdS/CuInS$_2$ nanoplates for excellent photocatalytic degradation performance and highly-efficient Cr(VI) reduction. Chem. Eng. J. 361, 1451–1461.

Dixit, S., Hering, J., 2003. Comparison of arsenic(V) and arsenic(III) sorption onto iron oxide minerals: implications for arsenic mobility. Environ. Sci. Technol. 37, 4182–4189.

Dong, X., Ma, L., Gress, J., Harris, W., Li, Y., 2014. Enhanced Cr(VI) reduction and As(III) oxidation in ice phase: important role of dissolved organic matter from biochar. J. Hazard. Mater. 267, 62–70.

Han, L., Zhong, Y., Su, Y., Wang, L., Zhu, L., Fei, X., Dong, Y., Hong, G., Zhou, Y., Fang, D., 2019. Nanocomposites based on 3D macroporous biomass carbon with SnS$_2$ nano-sheets hierarchical structure for efficient removal of hexavalent chromium. Chem. Eng. J. 369, 1138–1149.

Heng, H., Gan, Q., Meng, P., Liu, X., 2016. The visible-light-driven type III heterojunction H$_3$PW$_{12}$O$_{40}$/TiO$_2$-In$_2$S$_3$: a photocatalysis composite with enhanced photocatalytic activity. J. Alloy. Compd. 696, 51–59.

Huang, D., Li, J., Zeng, G., Xue, W., Chen, S., Li, Z., Deng, R., Yang, Y., Cheng, M., 2019. Facile construction of hierarchical flower-like Z-scheme AgBr/Bi$_2$WO$_6$ photocatalysts for effective removal of tetracycline: Degradation pathways and mechanism. Chem. Eng. J. 375, 121991.

Huo, X., Zhou, P., Zhang, J., Liu, Y., Cheng, X., Liu, Y., Li, W., Zhang, Y., 2020. N, S-doped porous carbon for persulfate activation to remove tetracycline: nonradical mechanism. J. Hazard. Mater. 391, 122055.

Imran, M., Iqbal, M.M., Iqbal, J., Shah, N.S., Khan, Z.U.H., Murtaza, B., Amjad, M., Ali, S., Rizwan, M., 2021. Synthesis, characterization and application of novel MnO and CuO impregnated biochar composites to sequester arsenic (As) from water: modeling, thermodynamics and reusability. J. Hazard. Mater. 401, 123338.

Jiang, W., Liu, Y., Zong, R., Li, Z., Yao, W., Zhu, Y., 2015. Photocatalytic hydrogen generation on bifunctional ternary heterostructured In$_2$S$_3$/MoS$_2$/CdS composite with high activity and stability under visible light irradiation. J. Mater. Chem. A 3, 18406–18412.

Jiang, X., Wang, L., Yu, F., Nie, Y., Xing, Q., Liu, X., Pei, Y., Zou, J., Dai, W., 2018. Photodegradation of organic pollutants coupled with simultaneous photocatalytic evolution of hydrogen using quantum-dot-modified g-C$_3$N$_4$ catalysts under visible-light irradiation. ACS Sustain. Chem. Eng. 6, 12695–12705.

Kläning, U.K., Bielski, B.H.J., Sehested, K., 1989. Arsenic(IV): a pulse-radiolysis study. Inorg. Chem. 28, 2717–2724.

Klüpfel, L., Keiluweit, M., Kleber, M., Sander, M., 2014. Redox properties of plant biomass-derived black carbon (biochar). Environ. Sci. Technol. 48, 5601–5611.

Kolarik, J., Prucek, R., Tucek, J., Filip, J., Sharma, V.K., Zboril, R., 2018. Impact of inorganic ions and natural organic matter on arsenates removal by ferrate(VI): understanding a complex effect of phosphates ions. Water Res. 141, 357–365.

Liu, Y., Mi, X., Wang, J., Li, M., Fan, D., Lu, H., Chen, X., 2019a. Two-dimensional SnS$_2$ nanosheets exfoliated from inorganic organic hybrid with enhanced photocatalytic activity towards Cr(VI) reduction. Inorg. Chem. Front. 6, 948–954.

Liu, G., Niu, P., Sun, C., Smith, S., Chen, Z., Lu, G., Cheng, H., 2010. Unique electronic structure induced high photoreactivity of sulfur-doped graphitic C$_3$N$_4$. J. Am. Chem. Soc. 132, 11642–11648.

Liu, Y., Pan, D., Xiong, M., Tao, Y., Chen, X., Zhang, D., Huang, Y., Li, G., 2020. In-situ fabrication SnO$_2$/SnS$_2$ heterostructure for boosting the photocatalytic degradation of pollutants. Chin. J. Catal. 41, 1554–1563.

Liu, F., Zhang, W., Tao, L., Hao, B., Zhang, J., 2019b. Simultaneously photocatalytic redox removal of chromium(VI) and arsenic(III) by hydrothermal carbon-sphere@ nano-Fe$_3$O$_4$. Environ. Sci. Nano 937–947 ,6 .

Li, Y., Chen, G., Wang, Q., Wang, X., Zhou, A., Shen, Z., 2010. Hierarchical ZnS-In$_2$S$_3$-CuS nanospheres with nanoporous structure: facile synthesis, growth mechanism, and excellent photocatalytic activity. Adv. Func. Mater. 20, 3390–3398.

Li, X., Jia, Y., Zhou, M., Su, X., Sun, J., 2020. High-efficiency degradation of organic pollutants with Fe, N co-doped biochar catalysts via persulfate activation. J. Hazard. Mater. 397, 122764.

Li, K., Yan, L., Zeng, Z., Luo, S., Luo, X., Liu, X., Guo, H., Guo, Y., 2014. Fabrication of H$_3$PW$_{12}$O$_{40}$-doped carbon nitride nanotubes by one-step hydrothermal treatment strategy and their efficient visible-light photocatalytic activity toward representative aqueous persistent organic pollutants degradation. Appl. Catal. B: Environ. 156–157, 141–152.

Li, Y., Zhang, B., Cheng, M., Li, Y., Hao, L., Guo, H., 2016. Spontaneous arsenic (III) oxidation with bioelectricity generation in single-chamber microbial fuel cells. J. Hazard. Mater. 306, 8–12.

Lohar, S., Sahana, A., Banerjee, A., Banik, A., Mukhopadhyay, S.K., Matalobos, J.S., Das, D., 2013. Antipyrine based arsenate selective fluorescent probe for living cell imaging. Anal. Chem. 85, 1778–1783.

Luo, J., Fu, K., Sun, M., Yin, K., Wang, D., Liu, X., Crittenden, J.C., 2019. Phase-mediated heavy metal adsorption from aqueous solutions using two-dimensional layered MoS$_2$. ACS Appl. Mater. Inter. 11, 38789–38797.

Lu, N., Zhao, Y., Liu, H., Guo, Y., Yuan, X., Xu, H., Peng, H., Qin, H., 2012. Design of polyoxometallate–titania composite film (H$_3$PW$_{12}$O$_{40}$/TiO$_2$) for the degradation of an aqueous dye Rhodamine B under the simulated sunlight irradiation. J. Hazard. Mater. 199–200, 1–8.

Meng, X., Bang, S., Korfiatis, G.P., 2000. Effects of silicate, sulfate, and carbonate on arsenic removal by ferric chloride. Water Res. 34, 1255–1261.

Moon, G., Kim, S., Cho, Y., Lim, J., Kim, D., Choi, W., 2017. Synergistic combination of bandgap-modified carbon nitride and WO$_3$ for visible light-induced oxidation of arsenite accelerated by in-situ Fenton reaction. Appl. Catal. B Environ. 218, 819–824.

Navarathna, C.M., Karunanayake, A.G., Gunatilake, S.R., Pittman, C.U., Perez, F., Mohan, D., Mlsna, T., 2019. Removal of arsenic(III) from water using magnetite precipitated onto Douglas fir biochar. J. Environ. Manag. 250, 109429.

Oh, W., Lisak, G., Webster, R., Liang, Y., Veksha, A., Giannis, A., Moo, J.G.S., Lim, J., Lim, T., 2018. Insights into the thermolytic transformation of lignocellulosic biomass waste to redox-active carbocatalyst: durability of surface active sites. Appl. Catal. B Environ. 233, 120–129.

Qu, Y., Xu, X., Huang, R., Qi, W., Su, R., He, Z., 2020. Corrigendum to "Enhanced photocatalytic degradation of antibiotics in water over functionalized N,S-doped carbon quantum dots embedded ZnO nanoflowers under sunlight irradiation" [Chem. Eng. J. 382 (2020) 123016]. Chem. Eng. J. 389, 123941.

Rahnemaie, R., Hiemstra, T., van Riemsdijk, W.H., 2007. Carbonate adsorption on goethite in competition with phosphate. J. Colloid Interf. Sci. 315, 415–425.

Roden, E., Kappler, A., Bauer, I., Jiang, J., Paul, A., Stoesser, R., Konishi, H., Xu, H., 2020. Extracellular electron transfer through microbial reduction of solid-phase humic substances. Nature 3, 417–421.

Sadeghi, M.H., Tofighy, M.A., Mohammadi, T., 2020. One-dimensional graphene for efficient aqueous heavy metal adsorption: rapid removal of arsenic and mercury ions by graphene oxide nanoribbons (GONRs). Chemosphere 253, 126647.

Shi, Y., Wang, X., Liu, X., Ling, C., Shen, W., Zhang, L., 2020. Visible light promoted Fe$_3$S$_4$ fenton oxidation of atrazine. Appl. Catal. B: Environ. 277, 119229.

Tian, W., Zhang, H., Duan, X., Sun, H., Tade, M., Ang, H., Wang, S., 2016. Nitrogen and sulfur-Co doped hierarchically porous carbon for adsorptive and oxidative removal of pharmaceutical contaminants. ACS Appl. Mater. Inter. 8, 7184–7193.

Wang, C., Luan, J., Wu, C., 2019. Metal-organic frameworks for aquatic arsenic removal. Water Res. 158, 370–382.

Wardman, P., 1989. Reduction potentials of one-electron couples involving free radicals in aqueous solution. J. Phys. Chem. Ref. Data 18, 1637–1755.

Wu, C., An, W., Liu, Z., Lin, J., Qian, Z., Xue, S., 2020. The effects of biochar as the electron shuttle on the ferrihydrite reduction and related arsenic (As) fate. J. Hazard. Mater. 390, 121391.

Wu, Z., Li, W., Webley, P.A., Zhao, D., 2012. General and controllable synthesis of novel mesoporous magnetic iron oxide@carbon encapsulates for efficient arsenic remova. Adv. Mater. 24, 485–491.

Wu, Y., Wang, H., Tu, W., Liu, Y., Wu, S., Tan, Y., Chew, J., 2018. Construction of hierarchical ^{2}D–^{2}D Zn3In2S6/fluorinated polymeric carbon nitride nanosheets photocatalyst for boosting photocatalytic degradation and hydrogen production performance. Appl. Catal. B: Environ. 233, 58–69.

Xi, Y., Zou, J., Luo, Y., Li, J., Li, X., Liao, T., Zhang, L., Wang, C., Lin, G., 2019. Performance and mechanism of arsenic removal in waste acid by combination of CuSO$_4$ and zero-valent iron. Chem. Eng. J. 375, 121928.

Xue, K., Wang, J., He, R., Yang, T., Yan, Y., Peng, Y., Omeoga, U., Wang, W., 2020. Photoredox catalysis of As(III) by constructed −C≡Sn−S bonds: using biomass as templates leads to bio-carbon/SnS$_2$ nanosheets capable of the efficient photocatalytic conversion of As(III) and calcium arsenate capture. Sci. Total. Environ. 732, 138963.

Xu, T., Kamat, P.V., O'Shea, K.E., 2005. Mechanistic evaluation of arsenite oxidation in TiO$_2$ assisted photocatalysis. J. Phys. Chem. A 109, 9070–9075.

Yang, C., Chang, J., Lee, D.J., 2020. Covalent organic framework EB-COF: Br as adsorbent for phosphorus (V) or arsenic(V) removal from nearly neutral waters. Chemosphere 253, 126736.

Ye, S., Yan, M., Tan, X., Liang, J., Zeng, G., Wu, H., Song, B., Zhou, C., Yang, Y., Wang, H., 2019. Facile assembled biochar-based nanocomposite with improved graphitization for efficient photocatalytic activity driven by visible light. Appl. Catal. B Environ. 250, 78–88.

Ye, S., Zeng, G., Tan, X., Wu, H., Liang, J., Song, B., Tang, N., Zhang, P., Yang, Y., Chen, Q., Li, X., 2020. Nitrogen-doped biochar fiber with graphitization from Boehmeria nivea for promoted peroxymonosulfate activation and non-radical degradation pathways with enhancing electron transfer. Appl. Catal. B Environ. 269, 118850.

Yi, X., Ma, S., Du, X., Zhao, C., Fu, H., Wang, P., Wang, C., 2019. The facile fabrication of 2D/3D Z-scheme g-C$_3$N$_4$/UiO-66 heterojunction with enhanced photocatalytic Cr (VI) reduction performance under white light. Chem. Eng. J. 375, 121944.

Zhang, S., Chen, L., Liu, H., Guo, W., Yang, Y., Guo, Y., Huo, M., 2012. Design of H$_3$PW$_{12}$O$_{40}$/TiO$_2$ and Ag/H$_3$PW$_{12}$O$_{40}$/TiO$_2$ film-coated optical fiber photoreactor for the degradation of aqueous rhodamine B and 4-nitrophenol under simulated sunlight irradiation. Chem. Eng. J. 200–202, 300–309.

Zhang, Y., Huang, Z., Shi, J., Guan, X., Cheng, C., Zong, S., Huangfu, Y., Ma, L., Guo, L., 2020. Maleic hydrazide-based molecule doping in three-dimensional lettuce-like graphite carbon nitride towards highly efficient photocatalytic hydrogen evolution. Appl. Catal. B Environ. 272, 119009.

Zhang, X., Li, X., Shao, C., Li, J., Zhang, M., Zhang, P., Wang, K., Lu, N., Liu, Y., 2013. One-dimensional hierarchical heterostructures of In$_2$S$_3$ nanosheets on electrospun TiO$_2$ nanofibers with enhanced visible photocatalytic activity. J. Hazard. Mater. 260, 892–900.

Zhang, Y., Thomas, A., Antonietti, M., Wang, X., 2009. Activation of carbon nitride solids by protonation: morphology changes, enhanced ionic conductivity, and photoconduction experiments. J. Am. Chem. Soc. 131, 50–51.

Zhu, W., Gao, J., Song, H., Lin, X., Zhang, S., 2019. Nature of the synergistic effect of N and S Co-doped graphene for the enhanced simultaneous determination of toxic pollutants. ACS Appl. Mater. Interfaces 11, 44545–44555.

Zuo, Y., Chen, J., Yang, H., Zhang, M., Wang, Y., He, G., Sun, Z., 2019. Facile synthesis of TiO$_2$/In$_2$S$_3$/CdS ternary porous heterostructure arrays with enhanced photoelectrochemical and visible-light photocatalytic properties. J. Mater. Chem. C. 7, 9065–9074.